Indirect Heat Flux Measurements at the Nozzle Throat of a Hybrid Rocket Motor

Pavan Narsai,[*] Edward Momanyi,[†] Krishna Venkataraman,[‡] Brian Evans,[§]
and Brian J. Cantwell[¶]

Stanford University, Stanford, CA, 94305 United States

Nozzle erosion in hybrid rocket motors is an unsolved problem that poses a hurdle to small-scale and long-burning hybrid rocket motor development. In studying nozzle erosion, it is immediately realized that heat transfer and heat flux into the nozzle material play a significant role in the throat regression phenomena. Furthermore, heat flux measurements at the throat could aid in the validation of CFD models currently being developed by other researchers. The purpose of this paper is to measure and analyze the inner surface heat flux experienced at the nozzle throat of a hybrid rocket motor.

Nomenclature

α	Thermal diffusivity	N	Total number of nodes
χ	Location of thermocouple	O/F	Oxidizer mass to fuel mass ratio
Δr	Grid spacing	P_0	Chamber pressure
Δt	Time step size	Pr	Prandtl number
γ	Ratio of specific heats	Q	Total number of thermocouples
λ	Guess heat flux	r	Radial coordinate
μ	Dynamic viscosity	r_c	Radius of curvature
ρ	Density	S	Number of future time steps
τ	Thermocouple measurement	s	Future time step number
θ	Minimization function	T	Temperature
A	Nozzle Area	t	Time
c^*	Characteristic exhaust velocity	Y	Numerical solution to heat equation
C_p	Isobaric specific heat capacity		
D	Nozzle diameter	*Subscripts*	
DAQ	Data Acquisition		
f	Applied heat flux	∞	Flow condition
g	Acceleration due to gravity	i	Thermocouple number
Gox	Gaseous oxygen	j	Index location
h_g	Estimated heat transfer coefficient	w	Wall condition
k	Thermal conductivity		
M	Mach number	*Superscripts*	
		$*$	At the throat location
		n	Time step

---

[*]PhD Candidate, Department of Aeronautics and Astronautics, 496 Lomita Mall Durand Building Room 051, Stanford CA 94305, and AIAA Member.

[†]BS Candidate, Department of Mechanical Engineering, 496 Lomita Mall Durand Building Room 051, Stanford CA 94305, and AIAA Member.

[‡]MS Candidate, Department of Aeronautics and Astronautics, 496 Lomita Mall Durand Building Room 051, Stanford CA 94305, and AIAA Member.

[§]Research Associate, Department of Aeronautics and Astronautics, 496 Lomita Mall Durand Building Room 051, Stanford CA 94305, and AIAA Senior Member.

[¶]Edward C. Wells Professor, Department of Aeronautics and Astronautics, 496 Lomita Mall, Durand Building Room 379, Stanford, CA 94305, and AIAA Fellow

American Institute of Aeronautics and Astronautics

I.   Introduction

DIRECTLY measuring the heating of a nozzle in a hybrid rocket motor is challenging because sensors cannot be placed on the inner wall surfaces of a nozzle and any direct attempts at measuring the heating rate would affect both the heating and the performance of the overall motor. It is therefore desired to attempt to indirectly measure the nozzle heating by using an approach, such as an inverse method.

Inverse heat transfer analysis is a desirable choice because it does not require a sensor at the surface of interest, and hence does not affect the heating rate nor the performance of the overall system. Furthermore, the sensors required are not exposed to the extreme environment of the flow. Instead, they are embedded within the nozzle wall material, where they experience high, but significantly lower temperatures than the temperatures inside of the flow path. Some difficulties with the inverse heat transfer solution lie within the fact that most nozzle materials do not have constant thermal properties. This is challenging because the resulting thermal behavior is nonlinear. The inverse heat transfer algorithm must then invert a nonlinear partial differential equation instead of a simple linear one, which can be computationally expensive. Furthermore, inverse heat transfer problems are a class of problems that are known to be ill-posed.[1] They do not have guaranteed unique solutions and effort must be taken to achieve stability. An inverse solver has been developed for the purposes of this study. This paper describes the development and testing of the solver as well as results from the solver using data taken from a manufactured hybrid rocket motor specifically for this research and comparisons of the results to Bartz' equation.[2]

A small-scale hybrid rocket motor has been developed to indirectly measure the heat flux experienced by the nozzle at the nozzle throat plane. This is achieved using embedded thermocouples at the nozzle throat plane. The long nozzle design utilized allows for a 1D heat transfer simplification. The propellants for the motor are gaseous oxygen (Gox) and paraffin wax, which are exhausted through the motor through a conical converging-diverging nozzle at a near-optimal expansion.

II.   Inverse Heat Transfer

Inverse heat transfer problems are a class of problems in which the definition of the problems are reversed. Common heat transfer problems provide geometry information as well as initial conditions and boundary conditions for all times of interest. The solutions to these problems are generally related to the resulting temperature profiles. Typical inverse problems instead provide an initial temperature estimate as well as a finite number of temperature measurements at discreet times and locations, leaving at least one of the boundary conditions as unknown. Generally, the solution of any inverse heat transfer problem is the determination of the unknown boundary conditions. The result of inverse solutions is not only the determination of the unknown boundary conditions, but also the full time-varying temperature profiles as well. These problems are considered difficult to solve because they are ill-posed–meaning a unique solution is not always guaranteed.[1]

Most inverse heat transfer solvers utilize knowledge of the direct heat transfer problem, knowledge of the material properties, and some sort of regularization to stabilize the solver. At the time of the research, the authors could not find a suitable inverse solver that solved the nonlinear heat equation in cylindrical coordinates with temperature-varying material properties. One was therefore developed and is described in this section.

The developed solver utilizes a semi-implicit direct solver which integrates the nonlinear one-dimensional heat equation in cylindrical coordinates that accounts for temperature-varying thermal properties. The solver starts off with estimated initial conditions and uses guess heat flux measurements with the direct solver to determine the best fit to the measured thermocouple data for every time step. For stability purposes, the future-time step with temporary assumption of linearly changing heat flux method is used as the objective function that is minimized with Brent's method.[3]

A.   Direct Heat Transfer Solution

The direct heat transfer solution utilized in the solver is based on the one-dimensional heat equation in cylindrical coordinates without generation, as shown in Equation 1. The arguments for reducing the heat equation to a single dimension are discussed in Section 3.D.

$$\frac{1}{r}\frac{\partial}{\partial r}(k(T)r\frac{\partial T}{\partial r}) = \rho Cp(T)\frac{\partial T}{\partial t} \tag{1}$$

American Institute of Aeronautics and Astronautics

After full expansion of the derivatives, it becomes apparent that the resulting partial differential equation is nonlinear, as shown in Equation 2, where the definition of thermal diffusivity has been used.

$$\alpha = \frac{k(T)}{\rho C_p(T)}$$

$$\alpha(T)\frac{\partial^2 T}{\partial r^2} + \frac{1}{r}\alpha(T)\frac{\partial T}{\partial r} + \frac{1}{\rho C_p(T)}\frac{\partial k(T)}{\partial T}\left(\frac{\partial T}{\partial r}\right)^2 = \frac{\partial T}{\partial t} \tag{2}$$

The semi-implicit Crank-Nicholson scheme is used to integrate Equation 2 instead of an explicit scheme because the heat equation is known to be very stiff.[4] Applying the Crank-Nicholson scheme with second order spatial discretization to Equation 2 results in Equation 3, where the temperature dependencies for α, k, and C_p have been dropped for convenience.

$$\frac{T_j^{n+1} - T_j^n}{\Delta t} =$$
$$\frac{1}{2}\left[\frac{\alpha^{n+1}}{\Delta r}T_{j+1}^{n+1}\left(\frac{1}{\Delta r} + \frac{1}{2r_j}\right) + \frac{\alpha^{n+1}}{\Delta r}T_j^{n+1}\left(-\frac{2}{\Delta r}\right) + \frac{\alpha^{n+1}}{\Delta r}T_{j-1}^{n+1}\left(\frac{1}{\Delta r} - \frac{1}{2r_j}\right) + \right.$$
$$\frac{1}{\rho C_p^{n+1}}\frac{dk}{dT}^{n+1}\left(\frac{T_{j+1}^{n+1} - T_{j-1}^{n+1}}{2\Delta r}\right)^2$$
$$+\frac{\alpha^n}{\Delta r}T_{j+1}^n\left(\frac{1}{\Delta r} + \frac{1}{2r_j}\right) + \frac{\alpha^n}{\Delta r}T_j^n\left(-\frac{2}{\Delta r}\right) + \frac{\alpha^{n+1}}{\Delta r}T_{j-1}^n\left(\frac{1}{\Delta r} - \frac{1}{2r_j}\right) +$$
$$\left.\frac{1}{\rho C_p^n}\frac{dk}{dT}^n\left(\frac{T_{j+1}^n - T_{j-1}^n}{2\Delta r}\right)^2\right] \tag{3}$$

Rearranging terms leads to Equation 4:

$$T_{j+1}^{n+1}\left(-c_{2,j}^{n+1}\right) + T_j^{n+1}\left(1 - c_{1,j}^{n+1}\right) + T_{j-1}^{n+1}\left(-c_{0,j}^{n+1}\right) - F_j^{n+1} = T_{j+1}^n\left(c_{2,j}^n\right) + T_j^n\left(1 + c_{1,j}^n\right) + T_{j-1}^n\left(c_{0,j}^n\right) + F_j^n \tag{4}$$

where

$$c_{2,j}^i = \frac{\Delta t\alpha(T_j^i)}{2\Delta r}\left(\frac{1}{\Delta r} + \frac{2}{r_j}\right)$$

$$c_{1,j}^i = \frac{\Delta t\alpha(T_j^i)}{2\Delta r}\left(\frac{-2}{\Delta r}\right)$$

$$c_{0,j}^i = \frac{\Delta t\alpha(T_j^i)}{2\Delta r}\left(\frac{1}{\Delta r} - \frac{2}{r_j}\right)$$

$$F_j^i = \frac{1}{\rho Cp(T^i)}\left.\frac{dk}{dT}\right|_{T=T_j^i}\left(\frac{T_{j+1}^i - T_{j-1}^i}{2\Delta r}\right)^2$$

Equation 4 holds for every grid point between j=2 and j=N-2. For the grid points j=1 and j=N-1, the boundary conditions are used, as shown in the following section.

1. Boundary Conditions

Equation 4 must be modified for nodes j=1 and j=n-1 to account for the boundaries of the grid. For the left side (j=1), the boundary condition is specified to be of a heat flux input (or a boundary condition of the second kind).[5]

$$f = -k\frac{\partial T}{\partial r}$$

When discretized, this becomes:

$$f = -k_1\frac{T_1 - T_0}{\Delta r}$$

American Institute of Aeronautics and Astronautics

Note the reduction of order for the spatial discretization. A modified spatial discretization scheme was not chosen for this boundary condition because it was desired to maintain a tridiagonal matrix. From here, it is possible to solve for T_0 and substitute into Equation 4 for $j = 1$:

$$T_0 = T_1 + \frac{f\Delta r}{k_1} \tag{5}$$

Substituting Equation 5 into Equation 4 for j=1 leads to a modified term in the matrix equation. For j=1, Equation 4 is then written as:

$$
\begin{aligned}
&T_2^{n+1}(-c_{2,1}^{n+1}) + T_1^{n+1}(1 - c_{1,1}^{n+1} - c_{0,1}^{n+1}) + \left(-F_1^{n+1} + \frac{f^{n+1}\Delta r}{k_1^{n+1}}(-c_{0,1}^{n+1})\right) \\
&= T_2^n(c_{2,1}^n) + T_1^n(1 + c_{1,1}^n) + \left(F_1^n + T_0^n(c_{0,1}^n)\right)
\end{aligned}
\tag{6}
$$

Note that the T_0 gets grouped with the F_1^n term and that the flux f does not show on the right hand side of equation because temperatures are known at all grid points at time step n.

For the right boundary condition, a known temperature is used. The result is that the T_n terms for both time steps n and n+1 get grouped with their respective F_{n-1} terms. For completeness, the modified Equation 4 for j = N-1 is written below:

$$
\begin{aligned}
&T_{N-1}^{n+1}(1 - c_{1,N-1}^{n+1}) + T_{N-2}^{n+1}(-c_{0,N-1}^{n+1}) + \left(-F_{N-1}^{n+1} + T_N^{n+1}(-c_{2,N-1}^{n+1})\right) \\
&= T_{N-1}^n(1 + c_{1,N-1}^n) + T_{N-2}^n(c_{0,N-1}^n) + \left(F_{N-1}^n + T_N^n(c_{2,N-1}^n)\right)
\end{aligned}
\tag{7}
$$

Note that T_N is known for both time steps n and n+1, as a thermocouple is expected to be placed on the back wall.

2. Thermal Properties

As it is desired to have an accurate solution to the direct heat transfer problem, it is necessary to have an accurate knowledge of the thermal properties and physical dimensions. For the analysis of this paper, a graphite nozzle is used with embedded thermocouples at various depths, as described in Section 3.D. GR001CC grade graphite is used and the thermal properties are measured to 1500C using Laser Flash Analysis (LFA) for thermal diffusivity, helium pycnometry for density, and Differential Scanning Calorimetry (DSC) for specific heat by Linseis. The accuracy of the LFA is rated to be 2.2% and the accuracy for the specific heat is 4%.[6] The thermal conductivity can then be inferred from the density, specific heat, and diffusivity.
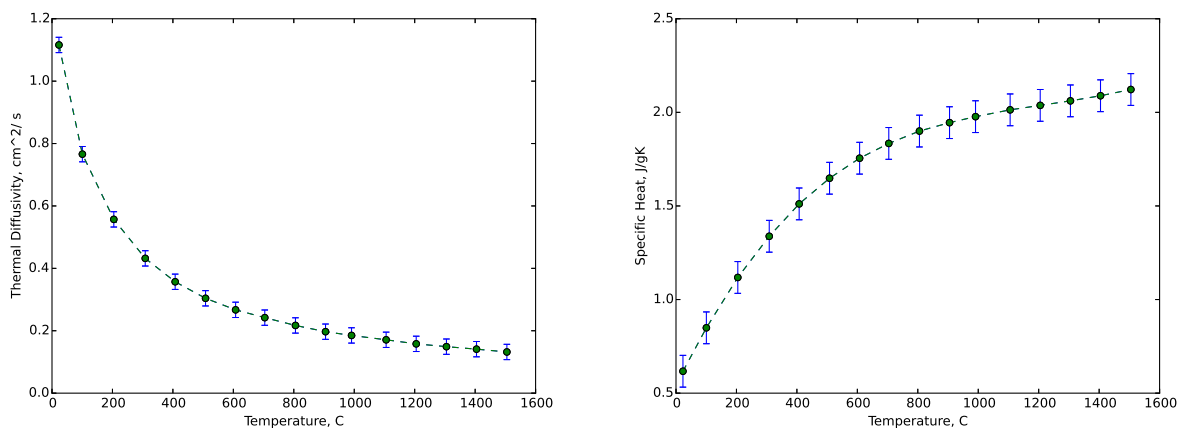

Figure 1. Thermal properties of graphite grade GR001CC

The material properties are extrapolated based on published data for temperatures above 1500C.[7] Although the density of graphite is practically constant[8] over the range of expected temperatures ($1.793 \ \frac{g}{cm^3}$),

American Institute of Aeronautics and Astronautics

the thermal diffusivity of the graphite material is measured to reduce by a factor of almost 10. This suggests that the non-linearity caused by the changing thermal properties plays a large role in the thermal response of the system.

3. Integrating the Direct Heat Equation

Considering Equations 4, 6, and 7 for every node between j=1 and j=N-1 leads to a tri-diagonal system.

$$
\begin{bmatrix}
(1 - c_{1,1}^{n+1} - c_{0,1}^{n+1}) & -c_{2,1}^{n+1} & 0 \\
-c_{0,j}^{n+1} & (1 - c_{1,j}^{n+1}) & -c_{2,j}^{n+1} \\
& \ddots & \ddots & \ddots \\
& & -c_{0,N-2}^{n+1} & (1 - c_{1,N-2}^{n+1}) & -c_{2,N-2}^{n+1} \\
& & 0 & c_{0,N-1}^{n+1} & (1 - c_{1,N-1}^{n+1})
\end{bmatrix}
\begin{pmatrix}
T_1^{n+1} \\
T_2^{n+1} \\
\vdots \\
T_{N-2}^{n+1} \\
T_{N-1}^{n+1}
\end{pmatrix}
+
$$

$$
\begin{pmatrix}
-F_1^{n+1} + \frac{f^{n+1}\Delta r}{k_1^{n+1}}(-c_{0,1}^{n+1}) \\
-F_2^{n+1} \\
\vdots \\
-F_{N-2}^{n+1} \\
-F_{N-1}^{n+1} + T_N^{n+1}(-c_{2,N-1}^{n+1})
\end{pmatrix}
=
$$

$$
\begin{bmatrix}
(1 - c_{1,1}^{n} - c_{0,1}^{n}) & -c_{2,1}^{n} & 0 \\
-c_{0,j}^{n} & (1 - c_{1,j}^{n}) & -c_{2,j}^{n} \\
& \ddots & \ddots & \ddots \\
& & -c_{0,N-2}^{n} & (1 - c_{1,N-2}^{n}) & -c_{2,N-2}^{n} \\
& & 0 & c_{0,N-1}^{n} & (1 - c_{1,N-1}^{n})
\end{bmatrix}
\begin{pmatrix}
T_1^{n} \\
T_2^{n} \\
\vdots \\
T_{N-2}^{n} \\
T_{N-1}^{n}
\end{pmatrix}
+
$$

$$
\begin{pmatrix}
-F_1^{n} + T_0^{n}(-c_{0,1}^{n}) \\
-F_2^{n} \\
\vdots \\
-F_{N-2}^{n} \\
-F_{N-1}^{n} + T_N^{n}(-c_{2,N-1}^{n})
\end{pmatrix}
$$

For convenience, this tridiagonal system is written as shown in Equation 8.

$$[\beta^{n+1}](T^{n+1}) + (F)^{n+1} = [\beta^n](T^n) + (F)^n \tag{8}$$

Note that for large r and constant thermal properties, this system collapses to the well known tridiagonal system for the linear heat equation in Cartesian coordinates.[4] For that case, unknown future time step temperatures can easily be solved for implicitly by solving the matrix equation. The addition of temperature-dependent thermal properties causes difficulties in that the coefficients inside of the tridiagonal matrix and the additional vector depend on future information. Therefore, a simple inversion procedure is not possible because the components of the key matrix are themselves unknown. To determine the future time step information, an iterative procedure must be implemented in addition to the solution of the matrix equation. The following procedure is utilized in the direct solution for the nonlinear heat equation:

1. (T^n) is known

2. Let $(T_{guess}) = (T^n)$ to start

3. Based on (T_{guess}), determine the tri-diagonal matrices

American Institute of Aeronautics and Astronautics

4. Solve Equation 8 for (T^{n+1}), which has the solution:

$$(T^{n+1}) = [\beta^{n+1}]^{-1} \left([\beta^n](T^n) + (F^n) - (F^{n+1})\right)$$

Where $[\beta^{n+1}]$ and (F^{n+1}) are based on (T_{guess}).

5. Compare (T_{guess}) and (T^{n+1})

6. If different, let $(T_{guess}) = (T^{n+1})$

7. Repeat from Step 3

8. If (T_{guess}) and (T^{n+1}) are equal within some tolerance, solution has converged and (T^{n+1}) is the converged solution

This scheme converges for most conditions. However, for very large changes in applied heat flux or large time steps, convergence fails or takes too many iterations. The failure is easily remedied by reducing the size of the particular time step.

4. Inverse Solution

Knowledge of the direct heat transfer solution is the most critical part of any inverse heat equation solver. For the developed solver, guess input heat fluxes are applied for each time step such that the computed profile and the experimental thermocouple data vary minimally. The most intuitive solution, where no regularization is used, has been shown to be unstable.[1] For stability, the developed solver uses future thermocouple data along with a temporary assumption that the heat flux changes linearly. Equation 9 shows the objective function for every time step that is minimized to determine the heat flux against time.

$$\theta = \sum_{s=1}^{S} \sum_{i=1}^{Q} \left(Y^{n+s}(s(\lambda^{n+1} - \lambda^n) + \lambda^n, \chi_i) - \tau_i^{n+s}\right)^2 \tag{9}$$

Where Y is the direct heat transfer solution. $Y^{n+s}(\lambda, \chi_i)$ is the temperature at location χ_i for the numerical solution profile at the n+s time step given λ heat flux at the final time step. τ_i^{n+s} refers to the ith thermocouple measurement at time step n+s. θ is the minimization term. It provides a measure of the difference between the temperature measurements and the numerical solver. In the given equation, the solver looks forward by S number of steps and there are a total of Q thermocouples present. For the experiment data and all analysis provided in this paper, 3 forward steps and 3 thermocouples are used, including the back wall thermocouple.

Equation 9 is minimized when the correct λ^{n+1} has been found. For the analysis in this paper, Brent's method from the Scientific Python package is used to minimize Equation 9.[3]

B. Numerical Simulations

Any inverse solver should always be tested using controlled numerical simulations so that one can understand how accurate the solver can determine heat fluxes against time. Also, the grid sizing and time step sizes need to be determined systematically as to reduce any unnecessary errors from building up during integration. This section describes the grid refinement, time-step size determination, and some inverse solution results against controlled numerical simulations.

1. Grid Refinement

As the direct heat transfer solution involves spatial discretization, high order terms are neglected. To ensure that these terms have minimal impact on the overall solution, it is necessary to know that the grid size allows only for acceptable error. This section describes how the number of grid points are selected for this experiment. For the following test, the relevant geometry is:

$$5mm \leq r \leq 25mm$$

American Institute of Aeronautics and Astronautics

and each of the refinement studies run for 1 second with an input heat flux of $1\frac{MW}{m^2}$, a predicted experimental value. The initial conditions are 300K everywhere, with the back wall maintained at 300K through the duration of the simulation.

The grid is refined based on the number of grid points and The time step used during the grid refinement study is $\Delta t = 0.001$ seconds, a value that is much smaller than needed. Figure 2 suggests that there is
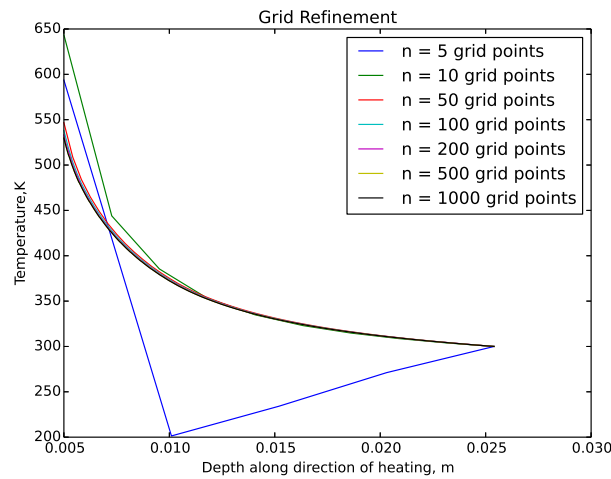

Figure 2. Temperature profiles after 1000 steps for various numbers of grid points.

relatively small gain for increasing the number of grid points over 50 grid points. There is also very large error in the profile when there are only 5 grid points. For the analysis in this paper, 100 grid points are used so that the inverse solver runs quickly and also ensures a relatively high degree of accuracy.

2. Time Step Refinement

In addition to refining the number of grid points, it is also important to refine the step size to achieve an acceptable error. For this study, various time step sizes are used for a 1 second simulation, and 510 grid points are used for the spatial discretization. The same flux and initial conditions are applied as in Section 2.1. The time step refinement study suggests that any step size smaller than 0.1 seconds should result in a
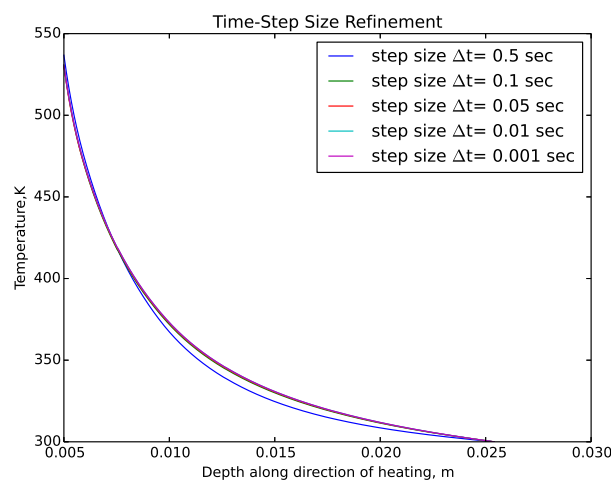

Figure 3. Temperature profiles after 1 second of simulation for various time step sizes.

negligible amount of discretization related errors. For the analysis in this paper, a step size of 0.02 seconds is selected.

American Institute of Aeronautics and Astronautics

3. Simple Inverse Solver Simulations

To understand the results of the inverse heat transfer analysis on the experimental data, it is important to first understand the nature of the solver and how it responds to simple numerical test cases. In this section, the inverse solver is tested against simple test cases and the results are explored. For each test, a defined heat flux profile is applied to the direct heat transfer solution and the resultant profile data is reduced down to simulated thermocouple data points. These thermocouple data points are then subjected to Gaussian noise and are fed into the inverse solver to determine the applied heat flux. The virtual thermocouples are located at 31% and 41% depths, as measured from the left wall. A virtual thermocouple is also placed at the back wall. These correspond to the physical locations where the thermocouples are installed in the experiment. The Gaussian noise that is applied corresponds to the error of the thermocouples.[9] The K-Type thermocouples used have accuracy of the larger of 1.1 C and 0.40% of the reading. For simplicity, 0.40% thermocouple error is used during the noise application.

The first test case the inverse solution is run against is a simple step change in applied heat flux. An applied heat flux of $10\frac{MW}{m^2}$ is applied at time $t = 1s$ and held there. Before one second, there is no applied heat flux. The results shown in Figure 4 suggests that the inverse solver works reasonably well. An important
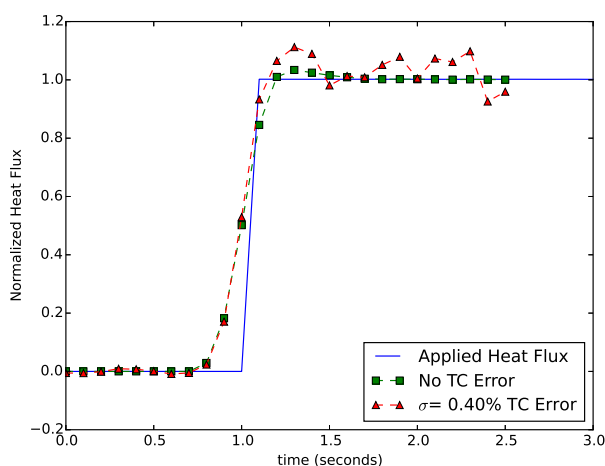

Figure 4. Inverse heat transfer solution for a simple step application of heat flux.

characteristic to note is that the estimated heat flux starts to increase before the actual step change in applied heat flux. This is expected as the inverse algorithm utilizes future data. Another consequence of the use of future data is that the inverse simulation must end before the thermocouple data runs out. The end result is that data needs to be collected for a few time steps after the end of shutdown to fully capture fire data during real experiments.

The second test case is similar to the first test, except two additional steps are applied. This test shows that the inverse solver is stable even when looking for negative heat fluxes and even larger changes in heat flux than before.

The third test is an inverted triangle test. Here, the heat flux is applied linearly to a maximum of 10 MW/m^2 and reduced back down to 0 MW/m^2. This simulation shows that the solver reacts much better to linearly changing heat fluxes as opposed to step changes. It also shows that the solver is robust against thermocouple errors and the resulting estimates are reliable, albeit a bit smoothed.
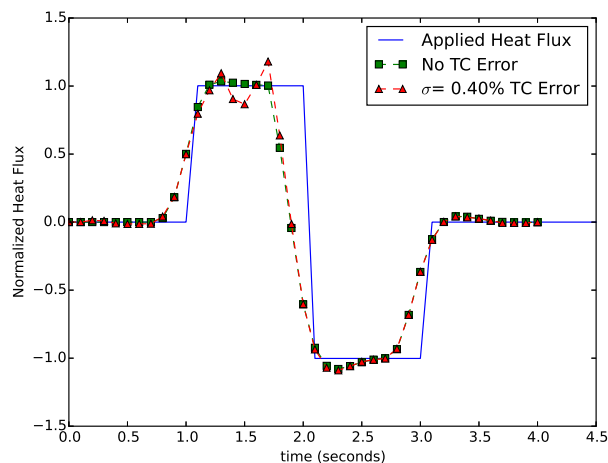
American Institute of Aeronautics and Astronautics

Figure 5. Inverse heat transfer solution for two applied step changes in heat flux.
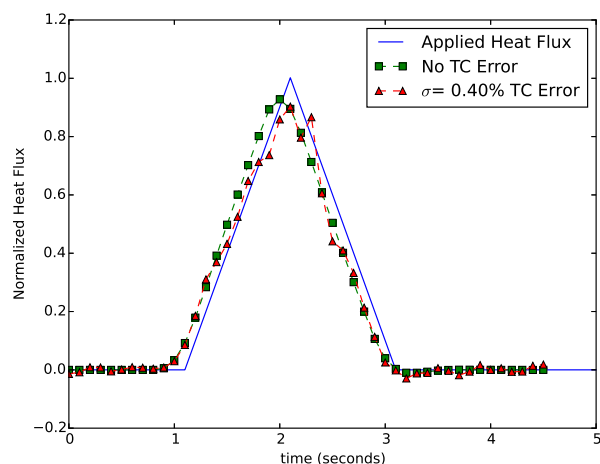

Figure 6. Inverse heat transfer solution for a simulation where the applied heat flux is linearly increased and then linearly decreased.

III. Experimental Setup

The fabricated hybrid rocket motor burns Gox and paraffin wax as propellants. A cross section view of the motor is provided in Figure 7. Key design elements of the motor include a sapphire window looking down the port of the motor, dual ignition capabilities, a mixing element, and a post combustion chamber for enhanced mixing. Furthermore, the motor has a modular design with the same thread pattern for all components and is capable of accepting future upgrades without the need for additional machining. The motor is equipped with two pressure transducers, four nozzle thermocouples, and an ultrasound sensor at the nozzle throat plane. The entire assembly is held together by thick mounting plates and tie rods.

A. Fore End

The fore end of the motor is brass and has 6 ports. Two ports intended for igniters are angled and pointed towards the location of the fuel grain. Ignition for the system is provided by a glow plug style initiator and a secondary slug, a combination similar to that used in the MATADOR project.[10] All six ports, including the inlet ports, are located on the sides of the fore end, as seen in Figure 7. This was deemed to be acceptable
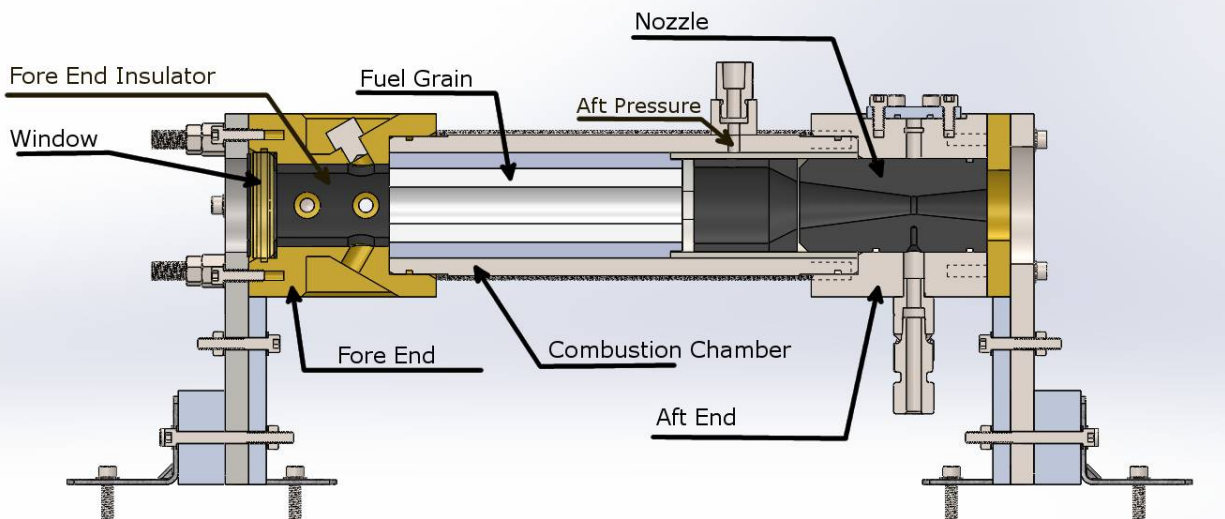
American Institute of Aeronautics and Astronautics

Figure 7. A cross section view of the experiment shows the components inside the motor.

as the only oxidizer expected to be used was Gox, which tends to be easier than other propellants because it is handled in a single phase. Four of the ports are currently used, while one of the igniter ports and one of the side ports remain open for future use. A small graphite tube was inserted into the flow path in the fore end to protect the brass from hot gas after Test #1. For the first test, a phenolic tube was used instead. Much of that tube burned away, which left a smokey and unstable-looking plume, as well as a higher average chamber pressure than expected. An optional sapphire window can be placed at the fore end of the motor to obtain a view down the port during fire. This window was installed for all tests starting with Test #4. The fore end is secured on the window side using a stainless steel 316 beam that is mounted down to an optics table.

B. Combustion Chamber

The combustion chamber casing is a thick-walled stainless steel tube with outer diameter of 7.62cm and an inner diameter of 5.72cm. The combustion chamber casing houses two insulators, a fuel grain, a mixer, a graphite post combustion chamber section, a graphite pre-nozzle ramp section, and part of the nozzle. It also has a welded bung which allows for a pressure transducer to be mounted in the aft combustion chamber region. The front insulator houses just a fuel grain and is thick walled to match the outer diameter of the fuel grain (3.96cm) and the inner diameter of the combustion chamber casing. The fuel grain has an inner diameter of 1.98cm and a length of 15.88cm, and is manufactured in the lab using a spin casting technique. The sizing of the fuel grain was done using the regression rates from previous research.[11] The mixer is an acrylic element which constricts the flow just downstream of the pure paraffin wax fuel grain. It is 0.64cm thick and has an inner diameter of 1.52cm. The combustion chamber assembly is held in place by the fore end and aft end sections of the motor.

C. Aft End

The aft end houses most of the sensors of interest for this study. It is a stainless steel block that houses the nozzle and has attachment points for plates to secure the nozzle and experiment in place. The aft end block has four large chamfers with port attachments on each face. This results in the aft end having the capability of having up to 7 embedded thermocouples in the nozzle and also the ability to use a delay line for an ultrasound transducer. The aft end is held up by a thick mounting plate on the back end. Figure 8 shows the aft end with sensors installed.
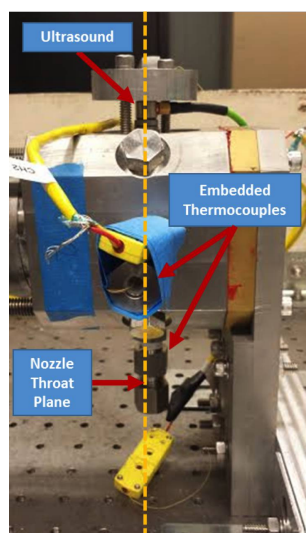
American Institute of Aeronautics and Astronautics

Figure 8. The aft end allows embedded thermocouples and an ultrasound sensor to be placed at the nozzle throat plane section.

D. Nozzle

It was desired to have the nozzle design mimic those of high performance motors, as this would lead to the most useful data. However, to reduce costs, the nozzle design is a simple conical converging-diverging nozzle. Nonetheless, this nozzle design is expected to have a 99% efficiency.[12] The throat diameter is 0.98cm, and the converging half-angle is $7.4°$ and the diverging half-angle is $5.6°$. The long nozzle design, which is longer than conventional nozzles, allows for a simplification to be made in the heat transfer analysis. Because of the long design, the heat transfer model is reduced from 3 dimensions to 2 dimensions. Furthermore, an angular symmetric argument can be made such that the problem is reduced to a single dimension.

There are 3 holes at the throat plane, as seen in Figure 10, to allow for embedded thermocouples. The depths are 31%, 41% and 51%. The last thermocouple is placed on the surface, which acts as an applied boundary condition for the inverse solver. During installation for the tests, thermocouple #3 (least deep) was broken and did not supply data. The analysis in all of this paper, including the simulations, take this into account and only use 3 thermocouples of data. Simulations with and without the 4th thermocouple data did not show much noticeable difference. Although embedding thermocouples into the nozzle breaks the angular symmetry, full three dimensional simulations show that the addition of thermocouples changes the thermal response negligibly.

The thermocouples are manufactured using a fine-wire welder from 50 micrometer diameter K-type thermocouple wire. It is desired to have a small thermocouple junction to reduce the response time.[13] The thermocouple wires are welded to insulated 75 micrometer diameter thermocouple wire and routed out of the aft end. These wires fed through sealed feedthroughs (WFS Series from Spectite)[14] and attached to a thermocouple connector. From there, shielded thermocouple extension wire is run to the thermocouple acquisition hardware. Figure 11 shows a manufactured thermocouple weld under a microscope.

Although it is generally desired to calibrate the thermocouples to their expected temperature environments, it is difficult to do so for the expected temperatures in the nozzle. Furthermore, the high temperatures can be damaging to the thermocouples themselves,[15] so calibration could potentially ruin the sensors. Instead, all of the manufactured thermocouples are verified at room temperature and at boiling water temperature, using the NIST conversion tables built into the thermocouple acquisition hardware.[16]

The thermocouples themselves are routed through protective ceramic tubes that are then potted into the graphite material using an electrically insulative paste manufactured by the Cotronics Corporation. This paste has relatively high thermal conductivity,[17] but still lower than that of graphite. This ultimately results in a loss of response time and accuracy for the thermocouples. Unfortunately, because graphite is electrically conductive, this loss seems inevitable. Better methods for potting in the thermocouples are being actively researched.

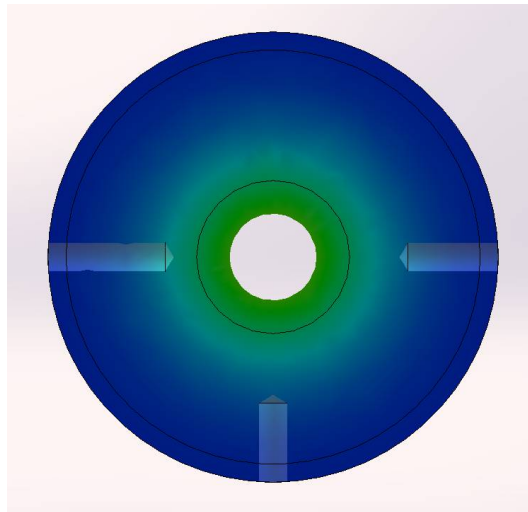American Institute of Aeronautics and Astronautics

Figure 9. Finite Element Simulations suggest that there is angular symmetry despite the fact that there are holes for embedded thermocouples at the throat plane.
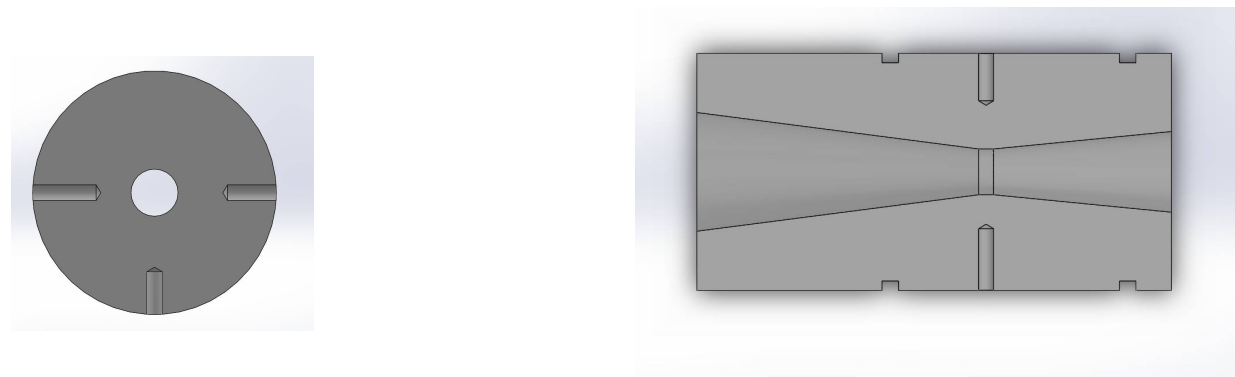

Figure 10. Nozzle cross sections shown in white for clarity. Note that the thermocouple holes are aligned with the nozzle throat plane.

E.   Feed System

Gox and nitrogen gas are fed to the motor from the feed system developed for the Stanford Combustion Visualization Facility.[18] The system was slightly modified to allow for isolation of both experiments. For convenience and mobility, quick disconnects and flexible tubing are used just upstream of the experiment. An actuated ball valve is placed just upstream of the injector to obtain the fastest open and close times. The main valve for oxygen has been measured to open in under a third of a second, and close in about one second. As done previously,[19] the flow within the feed system is choked through an orifice and the flow rate is measured using a venturi. Figure 12 shows the P&ID diagram utilized for the experiments. The driving pressure in the feed system is actively controlled by a dome-loaded regulator.

F.   Thermocouple Data Acquisition

Because of the nature of this study, it is desired to have accurate thermocouples as well as accurate data acquisition (DAQ) hardware. The thermocouple DAQ hardware is therefore isolated from all other measurements. A digital pin is used on the thermocouple DAQ hardware for timing purposes to align data between the other sensors from the experiment and feed system DAQ. The DAQ hardware used to record the thermocouple data is the USB 2408 device from the Measurement Computing Corporation.[16] It has an overall sample rate of up to 1kHz and features 24-bit resolution analog to digital converters for up to 8 thermocouples. For the analysis in this paper, all experiments were run with a thermocouple sample rate of
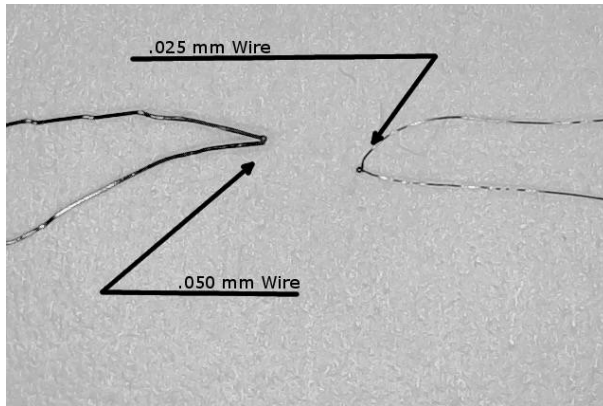
American Institute of Aeronautics and Astronautics

Figure 11. Examples of small wire thermocouples embedded in the nozzles. The left thermocouple is manufactured from 50 micrometer wire, while the right thermocouple is manufactured by Omega[9] from 25 micrometer wire. Note that the junction sizes are similar.
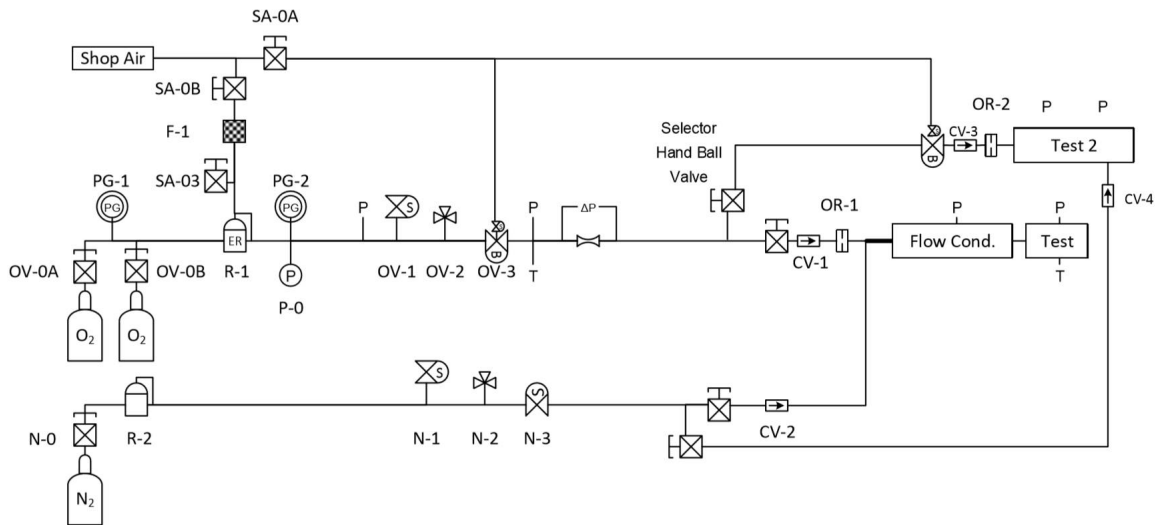

Figure 12. P&ID diagram of the feed system. Note that the experiment for this paper is labeled as Test 2 in the diagram.
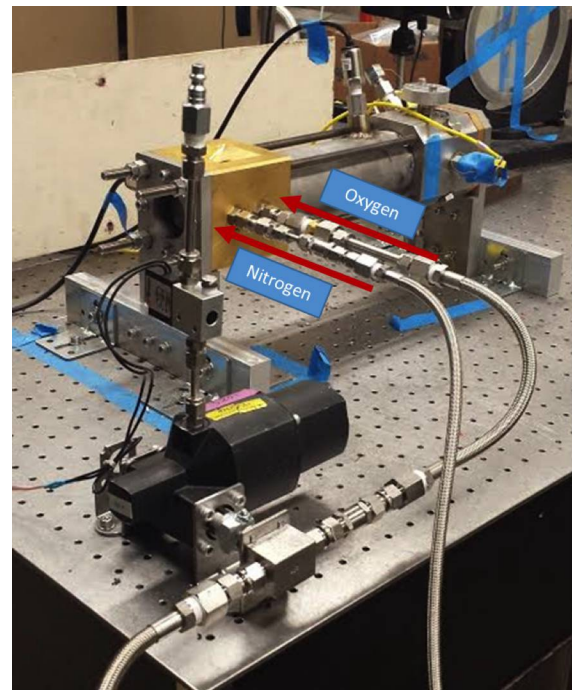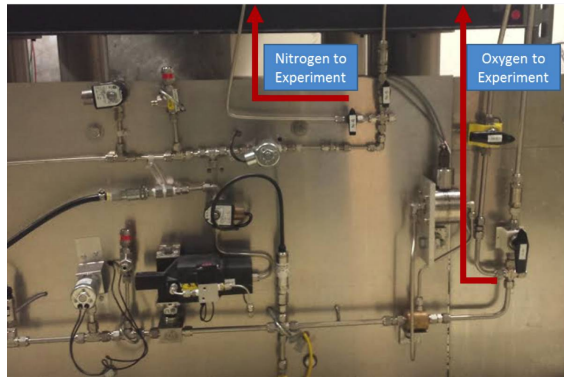
Figure 13. The feed system provides gaseous oxygen and nitrogen to the motor.

10Hz. Note that this is independent of the integration step size of 0.02 seconds.

IV. Experimental Results

The motor has completed it's first test campaign of five tests. These five tests had short burn times of about 2.5 seconds to start. The tests following the first test were reduced in duration for several reasons. The biggest reason was that a large amount of insulator material was burning at the fore end of the motor. This led to instabilities that were visually seen during the burn. The insulator in the fore end of the motor was subsequently changed to graphite and the modification resulted in a stable burn. Burn times for the following tests were reduced for the remainder of the test campaign nonetheless. Future tests will have longer burn times. The c^* efficiency is computed using measurements of the total amount of fuel burned, CEA[20] simulations based on the total amount of oxidizer and fuel burned, and the aft end pressure transducer data. The c^* efficiency was unexpectedly high during the first test. This is attributed to the insulator burning upstream of the fuel grain.

Table 1. Performance data for the tests

Test #	Burn Time (s)	Overall $\frac{O}{F}$ Ratio	Avg. Ox. Flow Rate (g/s)	Dia. Avg.[21] Flux ($\frac{kg}{m^2sec}$)	Avg. Chamber Pressure (MPa)	c^* Efficiency (%)
1	3.5	1.7	50.7	83.2	1.54	84
2	2.5	1.9	50.9	129.6	1.33	72
3	2.5	1.8	50.7	144.8	1.38	74
4	2.5	2.0	50.6	121.7	1.34	72
5	2.5	2.1	50.5	138.9	1.31	74

There are some hints of some swirl in the flow, likely due to the side injection scheme for the oxidizer. This injection scheme is likely what is also causing the fuel grain to burn in a non-uniform manner at the fore end of the grain, as shown in Figure 14. However, this irregular burning is only seen over a very short region of about a centimeter. The rest of the fuel grain seems to burn in a regular manner. The measurable data

American Institute of Aeronautics and Astronautics

Table 2. Estimated time-averaged heat flux at the nozzle throat plane for the tests.

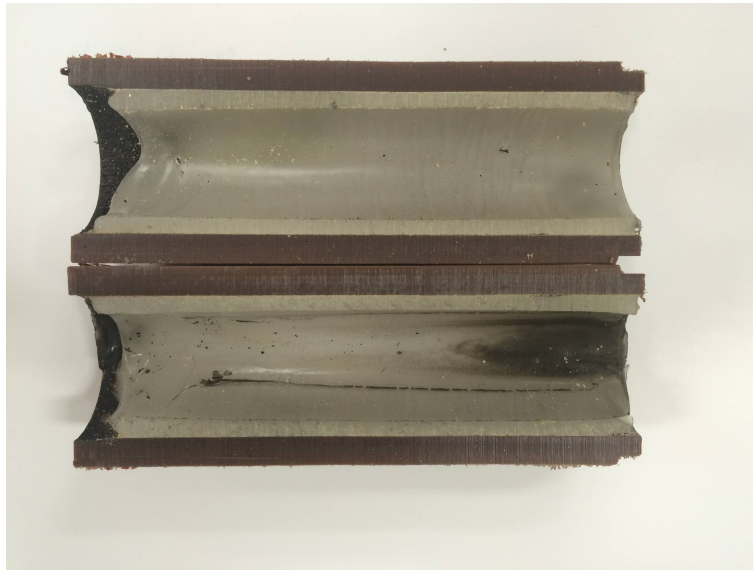| Test #	Avg. Heat Flux ($\frac{MW}{m^2}$)	Peak Heat Flux ($\frac{MW}{m^2}$)
1	–	–
2	35.27	37.57
3	32.57	35.16
4	34.84	37.20
5	34.21	36.49

Figure 14. The post fire fuel grain shows abnormal burning at the fore end. Some small angled waves can also be seen at the fore end, which hints at some swirl in the flow. Most of the fuel grain burns in a uniform manner.
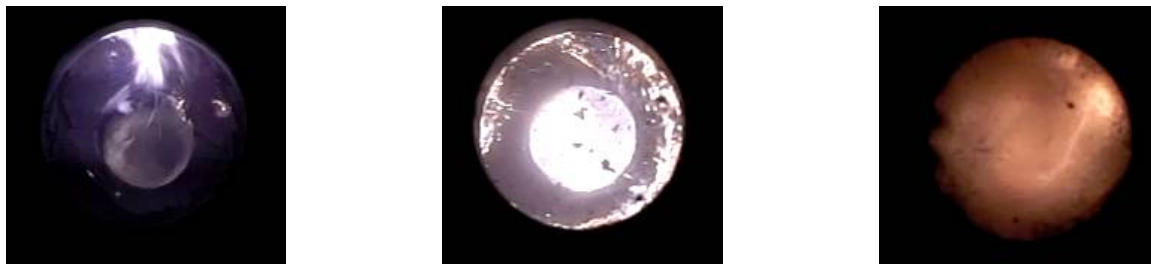

Figure 15. Still images taken from the window view during Test #5. The left image is captured just before the fuel grain starts burning. The middle is taken just after the fuel starts burning. Note that the inner diameter of the fuel grain is clearly visible. The right image, which is captured during shutdown, suggests that there is a small amount of swirl present in the flow.

(pressure and oxidizer flow rates) are consistent and the resulting estimated c^* efficiencies and average throat plane heat fluxes are also surprisingly consistent. Future tests with the same conditions are scheduled for different nozzles to determine whether the heat flux estimates remain consistent. The high speed video data and pressure trace data suggest that the motor runs in a very stable manner. Figure 16 shows pressure traces at the fore end and aft end of the motor. The difference between the fore end and aft end measurements is generally about 5%. This suggests that estimating c^* efficiency based on the fore end pressure measurements could increase the estimated efficiency of the motor by several percent. However, the more conservative aft end pressure measurements are used. The aft end pressure traces appear smoothed out compared to the fore
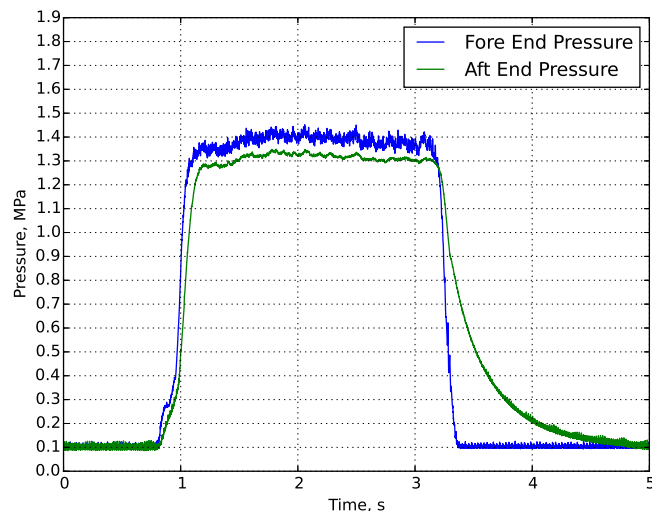
American Institute of Aeronautics and Astronautics

Figure 16. Pressure traces for Test #2. Note that the aft pressure sensor has a delayed response to shutdown due to the narrow flow path.

end traces and it also seems to show high pressure shortly after shutdown. This is due to the dampening nature of the flow path to the sensor, as seen in Figure 7. This narrow and indirect flow path protects the sensor from the hot gases generated from combustion. The active regulator in the feed system made it easy to dial in on the correct driving pressure to achieve the desired flow rates, which are all within 2% of each other.
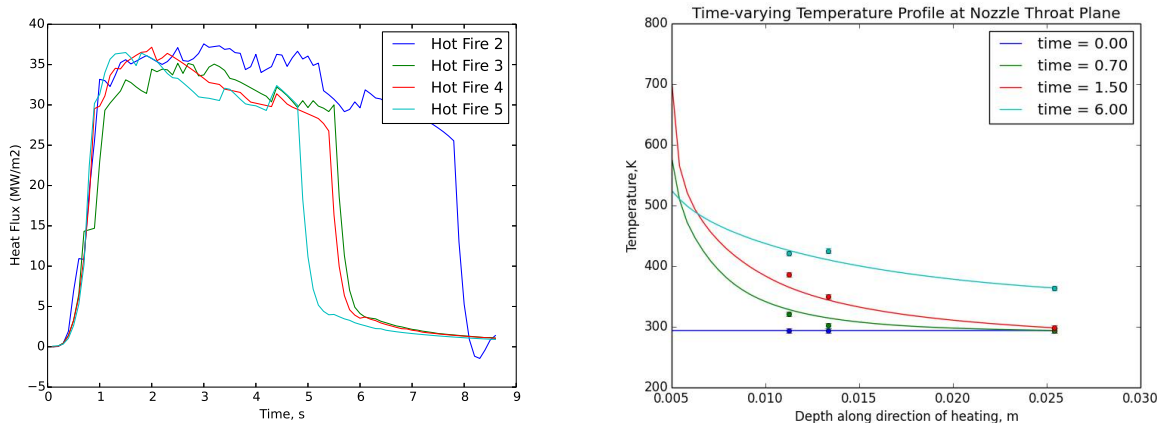

Figure 17. Indirect heat flux measurements for several tests are shown on the left. The comparison between estimated profiles and thermocouple data is shown on the right.

The indirectly estimated heat flux data seem to be very consistent between tests. They all peak near 35 $\frac{MW}{m^2}$. Also, the general trend for the heat flux is consistent with intuition. A large rise in flux is seen at the start up of the motor, after which it slowly decreases as the nozzle heats up. The results also show that the nitrogen purge starts at different times for each test, as expected because the time between purge and motor shutdown was varied between tests. It is noted that the flux estimations cannot determine the shutoff time of the motor. The applied heat flux tends to stay high between motor shutdown and the start of the nitrogen purge. This result was unexpected, as intuition suggests there would be a drop in applied heat flux at shutdown time. However, after shutoff, a flame persists out of the nozzle as the hot gases mix with the ambient air, as shown in Figure 18. Because of the location of this flame, the symmetric and one-dimensional arguments of the heat transfer model likely fail. This causes not only a loss in accuracy, but also puts the

American Institute of Aeronautics and Astronautics

solver at risk of going unstable. The heat flux estimations are therefore less accurate after shutoff time. Nonetheless, for each test, the estimated flux consistently remained high after shutdown until the nitrogen purge started. The purge did not immediately show negative flux as hot nitrogen was getting pushed out of the motor. Note that Test #1 did not have thermocouples in the motor as it was desired to first test fire the motor before studying heat transfer in the nozzle. Although the heat flux measurements are remarkably
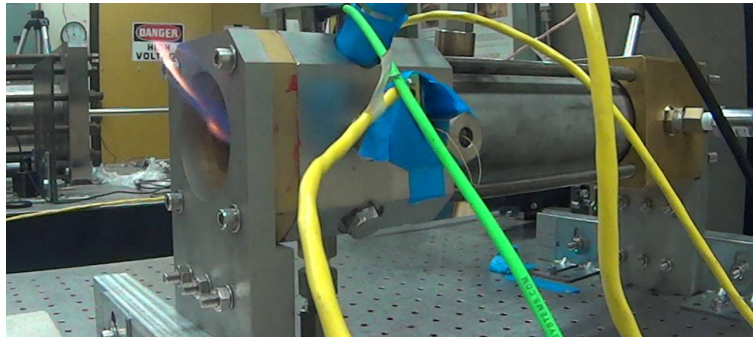

Figure 18. A residual flame is left at the end of the motor after the oxygen flow is turned off. The flame persists until the nitrogen purge is started.

similar, they do portray some differences during the fire and purge. This is expected because of the nature of the burning and errors in the locations of the thermocouples, the material properties, and the thermocouples themselves. Some differences include the rise time of the flux as well as some noisy oscillations. However, the most important quantity, the time-averaged heat flux, is consistent between tests at the design conditions. Future tests will have various O/F ratios as well as higher operating pressures to see how they change the applied heat flux at the nozzle throat. The comparison between the estimated temperature profiles is shown on Figure 17. The thermocouple data matches the profile data reasonably well, although not perfectly. This is due to uncertainty in material properties, temperature data, and the location of the thermocouples. It is also due to the forward stepping nature of the algorithm as well, which causes the profile to be ahead of the temperature measurements.
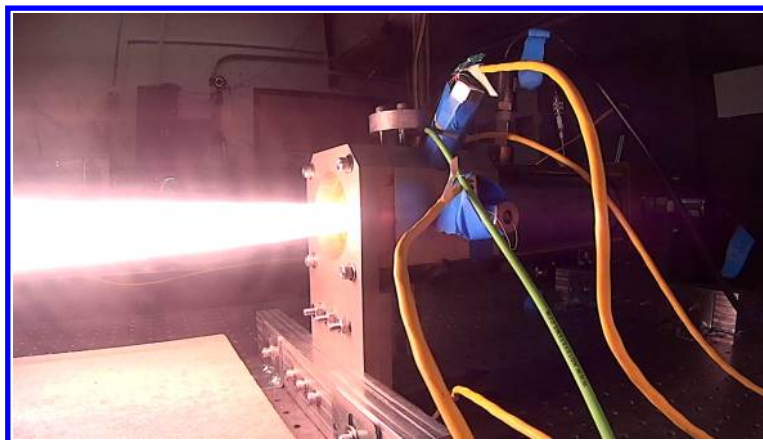

Figure 19. A view of the motor during Test #2.

The estimated heat flux data can be compared to Bartz'[2] equation for estimated heat transfer coefficients by using the simple definition of convective heat transfer.[5] Here, the initial wall temperature is used for T_w and 85% of the adiabatic flame temperature is used for T_∞. This simple conversion provides an estimated peak heat flux.

$$f = -h_g(T_w - T_\infty)$$

American Institute of Aeronautics and Astronautics

The convective heat transfer coefficient is given by Bartz as

$$h_g = \left[\frac{0.026}{D_*^{0.2}} \left(\frac{\mu^{0.26} C_p}{Pr^{0.6}} \right) \left(\frac{P_0 g}{c^*} \right) \left(\frac{D^*}{r_c} \right)^{0.1} \right] \left(\frac{A^*}{A} \right)^{0.9} \sigma$$

$$\sigma = \left[\left(\frac{\rho_{ref}}{\rho} \right) \left(\frac{\mu_{ref}}{\mu_0} \right)^{0.2} \right] = \frac{1}{\left[\frac{1}{2} \left(\frac{T_w}{T_0} \right) \left(1 + \frac{\gamma-1}{2} M^2 \right) + \frac{1}{2} \right]^{0.8-m/5} \left[1 + \frac{\gamma-1}{2} M^2 \right]^{m/5}}$$

(10)

Where m is taken to be 0.6.[2] The quantities, which are taken from CEA simulations and the physical experiment, are listed in Table 3 for convenience. Note that Equation 10 is for imperial units. After unit conversions, Bartz equation gives an approximate heat transfer coefficient of 16.6 $\frac{kW}{m^2 K}$ and in terms of heat flux, 41.5 $\frac{MW}{m^2}$, which is remarkably close to the experimental values. Furthermore, if the pressure value is replaced with the average chamber pressure value realized experimentally (1.34 MPA), the heat flux estimated by Bartz' equation reduces to 33.9 $\frac{MW}{m^2}$ which is nearly identical to the experimental values! This suggests that, at least for the design conditions, Bartz' equation provides a very good approximation to the heat flux experienced at the nozzle throat.

Table 3. Values used in determining the approximate heat flux given by Bartz' equation.

Term	Value	Units
D_*	0.0099	m
μ	1.0669×10^{-4}	$\frac{kg}{ms}$
c_p	7.885	$\frac{kJ}{kgK}$
Pr	0.4582	–
P_0	1.7237	MPa
g	9.81	$\frac{m}{s^2}$
c^*	1807	$\frac{m}{s}$
r_c	.005	m
$\frac{A^*}{A}$	1	–
$\frac{T_w}{T_0}$	0.85	–
γ	1.1309	–
M	1	–

V. Future Work

As the inverse solver has proven to be stable and consistent for O/F ratios around two at chamber pressures of 1.38 MPa, it is desired to see how inner heat flux estimations change with varying O/F ratios and chamber pressures and if they remain close to approximations by Bartz.[2] It is also desired to change the fuel to a slow burning fuel such as acrylic to test the algorithm's stability over long burn times. Future enhancements to the experiment's procedures include better methods to install embedded thermocouples in the nozzles, as well as optimized purge times to minimize the error caused by the residual flame after Gox shutoff.

VI. Conclusion

A nonlinear inverse heat transfer algorithm has been developed to estimate the heat flux experienced at the throat plane of a hybrid rocket motor. To test the algorithm, a small-scale hybrid rocket motor was built with high-performance design considerations. The motor firings to date have been stable and have provided consistent nozzle throat heat flux estimations. Remarkably, these estimations are nearly identical to approximate heat flux estimations obtained from Bartz' equation.[2]

American Institute of Aeronautics and Astronautics

VII.   Acknowledgments

References

[1]Beck, J., Blackwell, B., and St. Clair, C. J., *Inverse Heat Conduction, Ill-posed Problems*, John Wiley & Sons, Inc., 1985.

[2]Bartz, D., *Turbulent Boundary-Layer Heat Transfer From Rapidly Accelerating Flow of Rocket Combustion Gases and of Heat Air*, California Institute of Technology, 1963.

[3]Community, T. S., "scipy.optimize.brent," 2015.

[4]Moin, P., *Fundamentals of Engineering Numerical Analysis*, Cambridge University Press, 2010.

[5]Incropera, F., D., D., Bergman, T., and Lavine, A., *Fundamentals of Heat and Mass Transfer*, John Wiley & Sons, Inc., 2007.

[6]Linseis, "LFA 1000/1000 HT, Thermal Diffusivity & Thermal Conductivity," 2015.

[7]Uher, C., "4.3.2 Temperature dependence of thermal conductivity of graphite," *Thermal Conductivity of Pure Metals and Alloys*, edited by O. Madelung and G. White, Vol. 15c of *Landolt-Brnstein - Group III Condensed Matter*, Springer Berlin Heidelberg, 1991, pp. 430–439.

[8]Page, D., *The Industrial Graphite Engineering Handbook*, UCAR Carbon Co., 1991.

[9]Omega Engineering Inc., "Thermocouples," http://www.omega.com/thermocouples.html, 2015, Accessed: January 5, 2015.

[10]Lohner, K., Dyer, J., Doran, E., Dunn, Z., and Zilliac, G., *Fuel Regression Rate Characterization Using a Laboratory Scale Nitrous Oxide Hybrid Propulsion System*, American Institute of Aeronautics and Astronautics, 2015/07/02 2006.

[11]Zilliac, G. and Karabeyoglu, M., *Hybrid Rocket Fuel Regression Rate Data and Modeling*, American Institute of Aeronautics and Astronautics, 2015/07/02 2006.

[12]Sutton, G. and Biblarz, O., *Rocket Propulsion Elements*, John Wiley & Sons, Inc., 2010.

[13]Omega Engineering, Inc., "Thermocouple Response Time," http://www.omega.com/temperature/Z/ThermocoupleResponseTime.html, 2015, Accessed: January 5, 2015.

[14]Spectite Inc., "Series WF Feedthroughs," http://spectite.com/wf.html, 2015, Accessed: June 5, 2015.

[15]Omega Engineering Inc., "Reference Guide," http://www.omega.com/temperature/pdf/tc˙temp˙limits˙range.pdf, 2015, Accessed: June 5, 2015.

[16]Measurement Computing, "USB 2408 Series," http://www.mccdaq.com/usb-data-acquisition/USB-2408-Series.aspx, 2015, Accessed: June 5, 2015.

[17]Cotronics Corp., "Special Purpose Hi-Temp Adhesives," http://www.cotronics.com/catalog/28Jan 12, 2015.

[18]Chandler, A., Jens, E., Cantwell, B., and Hubbard, G. S., *Visualization of the Liquid Layer Combustion of Paraffin Fuel for Hybrid Rocket Applications*, American Institute of Aeronautics and Astronautics, 2015/07/02 2012.

[19]Jens, E. T., Chandler, A. A., Cantwell, B., Hubbard, G. S., and Mechentel, F., *Combustion Visualization of Paraffin-Based Hybrid Rocket Fuel at Elevated Pressures*, American Institute of Aeronautics and Astronautics, 2015/07/02 2014.

[20]Snyder, C. A., "Chemical Equilibrium with Applications," http://www.grc.nasa.gov/WWW/CEAWeb/ceaHome.htm, 2015, Accessed: June 5, 2015.

[21]Karabeyoglu, A., Cantwell, B., and Zilliac, G., *Development of Scalable Space-Time Averaged Regression Rate Expressions for Hybrid Rockets*, American Institute of Aeronautics and Astronautics, 2015/07/02 2005.

American Institute of Aeronautics and Astronautics

This article has been cited by:

1. Lingfei He, Hui Tian, Ruipeng Yu, Sheng Zhao, Pengfei Wang, Yuanjun Zhang. 2021. Transient investigation of nozzle erosion in a long-time working hybrid rocket motor. *Aerospace Science and Technology* 106978. [Crossref]

2. Giuseppe Leccese, Enrico Cavallini, Marco Pizzarelli. State of Art and Current Challenges of the Paraffin-Based Hybrid Rocket Technology . [Citation] [PDF] [PDF Plus]

3. Taiping Wang, Bing Sun, Di Liu, Jixin Xiang. 2018. Experimental investigation of two-dimensional wall thermal loads in the near-injector region of a film-cooled combustion chamber. *Applied Thermal Engineering* **138**, 913-923. [Crossref]

4. Giuseppe Leccese, Daniele Bianchi, Francesco Nasuti, Keith J. Stober, Pavan Narsai, Brian J. Cantwell. Simulations of Paraffin-Based Hybrid Rocket Motors and Comparison with Experiments . [Citation] [PDF] [PDF Plus]

5. Keith J. Stober, Pavan Narsai, Krishna Venkataraman, Anna Thomas, Brian J. Cantwell. Flame Emission Spectroscopy in a Paraffin-Based Hybrid Rocket . [Citation] [PDF] [PDF Plus]